Phonon effects in quantum dot single-photon sources

Denning, Emil V.; Iles-Smith, Jake; Gregersen, Niels; Mork, Jesper

Published in:
Optical Materials Express

Link to article, DOI:
10.1364/OME.380601

Publication date:
2020

Document Version
Publisher's PDF, also known as Version of record

Research Article | Vol. 10, No. 1 / 1 January 2020 / Optical Materials Express 222
Optical Materials EXPRESS

Phonon effects in quantum dot single-photon sources

EMIL V. DENNING,[1] JAKE ILES-SMITH,[2] NIELS GREGERSEN,[1] AND JESPER MORK[1,*]

[1]Department of Photonics Engineering, DTU Fotonik, Technical University of Denmark, Building 343, 2800 Kongens Lyngby, Denmark
[2]Department of Physics and Astronomy, University of Sheffield, Sheffield S3 7RH, UK
[*]jesm@fotonik.dtu.dk

Abstract: Semiconductor quantum dots are inevitably coupled to the vibrational modes of their host lattice. This interaction reduces the efficiency and the indistinguishability of single-photons emitted from semiconductor quantum dots. While the adverse effects of phonons can be significantly reduced by embedding the quantum dot in a photonic cavity, phonon-induced signatures in the emitted photons cannot be completely suppressed and constitute a fundamental limit to the ultimate performance of single-photon sources based on quantum dots. In this paper, we present a self-consistent theoretical description of phonon effects in such sources and describe their influence on the figures of merit.

1. Introduction

Sources of single indistinguishable photons are key components in optical quantum information processing [1], and deterministic single-photon sources based on self-assembled semiconductor quantum dots (QDs) have developed significantly over the past few years. QDs can be grown with excellent optical properties, and advances in fabrication of photonic nanostructures have led to demonstrations of bright and coherent single-photon sources [2–5]. However, the inevitable coupling of the QD to the vibrational phonon modes of the host lattice constitutes a significant challenge [6], which will only be increasingly important as the performance of the sources is pushed from the current state-of-the-art towards the high level necessary for realising large-scale optical quantum computation.

There are several figures of merit that characterise the performance of a single photon source. Naturally, the photon number statistics of the emitted light is important. The Hanbury Brown and Twiss second-order correlation function, $g^{(2)}(\tau)$, quantifies the probability of simultaneously detecting two photons when evaluated at $\tau = 0$ [8]. Multiphoton components in the emitted light leads to a non-zero value of $g^{(2)}(0)$, which can stem from the excitation process [9–11]. Similarly, the efficiency of the source is the probability of sending a single photon into the detection channel when the source is triggered [7]. Another important feature, which characterises the coherence properties of the source, is the indistinguishability of the emitted photons, which is a measure of the degree to which two photons can interfere. The indistinguishability is measured by sending the two photons into the two input ports of a beamsplitter. If the two photons are completely indistinguishable, the Hong-Ou-Mandel effect results in the photons leaving the beamsplitter in the same output port [12]. This effect is a fundamental necessity for linear quantum computing schemes, forming the basis for two-photon gates [13]. Alternatively, the quantum dot can be operated by exciting a biexciton, thereby emitting a polarisation-entangled photon pair [4,14,15]. In this scenario, the entanglement fidelity of the emitted photon pair constitutes an additional figure of merit of the source. Suppressing phonon-assisted photon emission in these pair-sources requires individual, polarisation-degenerate Purcell enhancement of the exciton and biexciton lines, which relies on highly challenging photonic engineering [16].

#380601 https://doi.org/10.1364/OME.380601
Journal © 2020 Received 17 Oct 2019; revised 6 Dec 2019; accepted 11 Dec 2019; published 23 Dec 2019

Optical Materials EXPRESS

The focus of the present paper is the impact of phonons on the efficiency and indistinguishability in the context of single-photon generation. Phonons influence these figures of merit by 1) generating detuned, distinguishable photons in a sideband by exchanging energy with the QD [17–20] and 2) dephasing the QD exciton through scattering of thermal phonons [21–23]. When the QD relaxes from its excited state to its ground state, a phonon wavepacket can be simultaneously created, thereby leading to the emission of a photon with energy lower than that of the QD exciton (see Fig. 1(a)). The precise energy of the photon is not known, since it depends on the energy of the phonon wavepacket, which is lost into the environment. As a result, photons produced through this phonon-mediated transition are inherently distinguishable. Similarly, if the temperature is high enough to allow for thermal population of the phonon modes, a phonon wavepacket can be absorbed, leading to emission of a blue-detuned photon. In the emission spectrum of the source, these processes are observed as a broad sideband in the vicinity of a narrow zero-phonon line, corresponding to a phononless $|e\rangle \rightarrow |g\rangle$ transition (see Fig. 1(b)). Furthermore, if the thermal occupation of phonon modes is appreciable, thermal phonons can interact with the QD and drive virtual transitions to higher excited states. Although such scattering processes do not induce population transfer, they dephase the dipole moment of the QD during the photon emission process [21], which also leads to a decrease in the photon indistinguishability [23]. This effect can be suppressed simply by operating the source at temperatures far below the characteristic phonon energies.

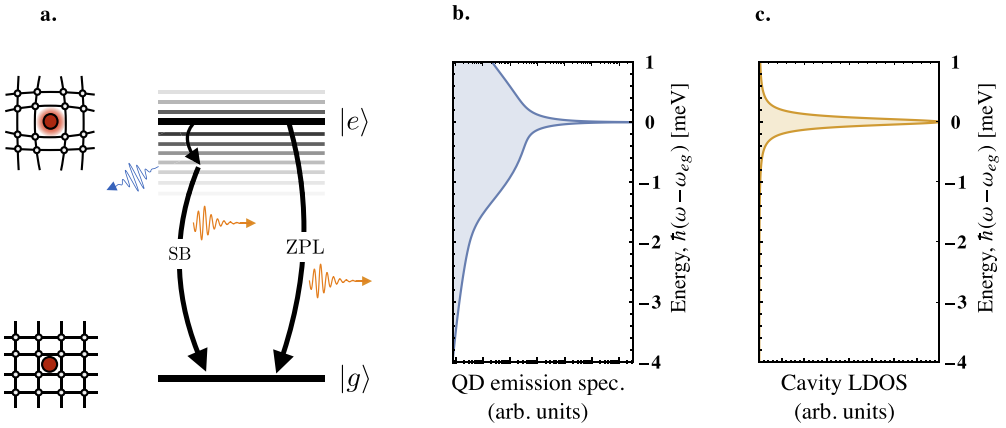

Fig. 1. **a.** When a quantum dot decays from its lowest-lying exciton state, $|e\rangle$, to its ground state, $|g\rangle$, a phonon wavepacket may be emitted or absorbed. This leads to a broad sideband (SB) in the photon emission spectrum along with the narrow zero-phonon line (ZPL), arising from relaxation not involving phonons. **b.** Emission spectrum showing the sideband and zero-phonon line. The emission spectrum has been calculated with a polaron master equation, described in Sec. 3. **c.** By introducing a cavity with narrow linewidth, the zero-phonon line can be selectively enhanced through the Purcell effect. Here, the optical spectral density of a Fabry-Pérot cavity, Eq. (5), is shown.

Naturally, the incoherent photons can be removed by applying a narrow filter around the coherent zero-phonon line in the spectrum, which is done in most indistinguishability measurements on single-photon sources, e.g. Refs. [2,5]. Although restoring the indistinguishability, such filtering will also decrease the efficiency of the source. The fraction of photons emitted into the phonon sideband can also be reduced by placing the QD in a photonic cavity with a narrow resonance line that selectively enhances zero-phonon emission processes through the Purcell effect (see Fig. 1(c)). However, this funneling strategy only works up to the limit where the Purcell regime breaks down and strong light–matter coupling sets in. In the strong-coupling regime, a relaxation

Optical Materials EXPRESS

from the upper to the lower polariton state can occur by emitting a phonon wavepacket, thereby reducing the coherence of the system and the indistinguishability of the emitted photons [24]. Furthermore, in the entangled photon pair application, a single broadband Purcell enhancement [4] covering both the exciton and biexciton lines cannot be used to suppress the phonon sideband. Here, the funneling strategy would require a twin-cavity approach [16].

The vibrational environment is not the only important noise mechanism that degrades the single-photon coherence. Another dominant mechanism is the slow charge fluctuations in nearby crystal impurities [23,25] and fluctuations in the local nuclear spins [26–28]. Since the typical time scale of these fluctuations can be as slow as a few tens of kHz they do not necessarily degrade the indistinguishability of photons emitted subsequently from the same source [3]. However, when multiple single-photon sources are used in combination, the charge fluctuations in two distinct sources are completely uncorrelated, and thus the photons become distinguishable [29].

An additional source of decoherence is the timing jitter introduced by non-resonant or quasi-resonant excitation schemes [30,31]. In these excitation schemes, the stochastic relaxation process from a higher excited state to the lowest-energy exciton via nonradiative processes leads to an uncertainty in the emission time, which degrades the Hong-Ou-Mandel interference visibility. However, by using strictly resonant excitation, this problem can be largely overcome [32–34].

In this paper, we focus on the influence of phonon interactions on the emission properties of QD single photon sources. Further, the effect of a structured electromagnetic environment is included as a central feature of our analysis. Thus, we will consider a total Hamiltonian of the form

$$H = H_{\mathrm{E}} + H_{\mathrm{P}} + H_{\mathrm{F}} + H_{\mathrm{EP}} + H_{\mathrm{EF}}, \tag{1}$$

where $H_{\mathrm{E}} = \hbar\omega_{eg}|e\rangle\langle e|$ is the free evolution of the emitter (with $|g\rangle$ and $|e\rangle$ denoting the ground state and lowest exciton state, respectively, separated by an energy $\hbar\omega_{eg}$), H_{F} and H_{P} describe the free evolution of the electromagnetic field and phonon environment, respectively and H_{EF} and H_{EP} describe the interaction of these environments with the emitter. In the following sections we will describe all environmental terms in the Hamiltonian in detail and derive the fundamental properties of light emitted from the system.

2. Properties and numerical model for the photonic structure

To control the light emission and ensure a good coupling to the collection optics, the QD is typically placed in a photonic structure. Such structures often fall in two categories: A waveguide or a cavity. A waveguide offers highly directional emission and broadband screening of the optical radiation modes, which increases the overall efficiency of the source, but not the indistinguishability due to lack of spectral selectivity. Cavities with linewidths below the frequency range of the sideband selectively funnels emission into the zero-phonon line, thereby increasing the indistinguishability. Simultaneously, the efficiency is increased due to Purcell enhancement.

Many nanophotonic cavities are essentially realized by adding a pair of mirrors to an underlying waveguide. The waveguide as well as the mirrors can be implemented in various ways and have different characteristics, but we will here treat the cavity using a unified framework (see Fig. 2(a)) allowing analysis of many different geometries. One example is the micropillar configuration, where the central cavity section is an unstructured, waveguide, while distributed Bragg reflectors (DBRs) constitute the mirrors (see Fig. 2(b)). Another example is a line-defect photonic crystal cavity, where a missing row of air holes constitutes a line-defect waveguide and the re-instated holes form the mirrors. The waveguide structure is characterised by a spontaneous emission rate into the fundamental mode, Γ_0, and the effective index of this mode, $\bar{n}$, while the cavity is formed by adding two mirrors with amplitude reflectivities r_1 and r_2, separated by a distance L.

Optical Materials EXPRESS

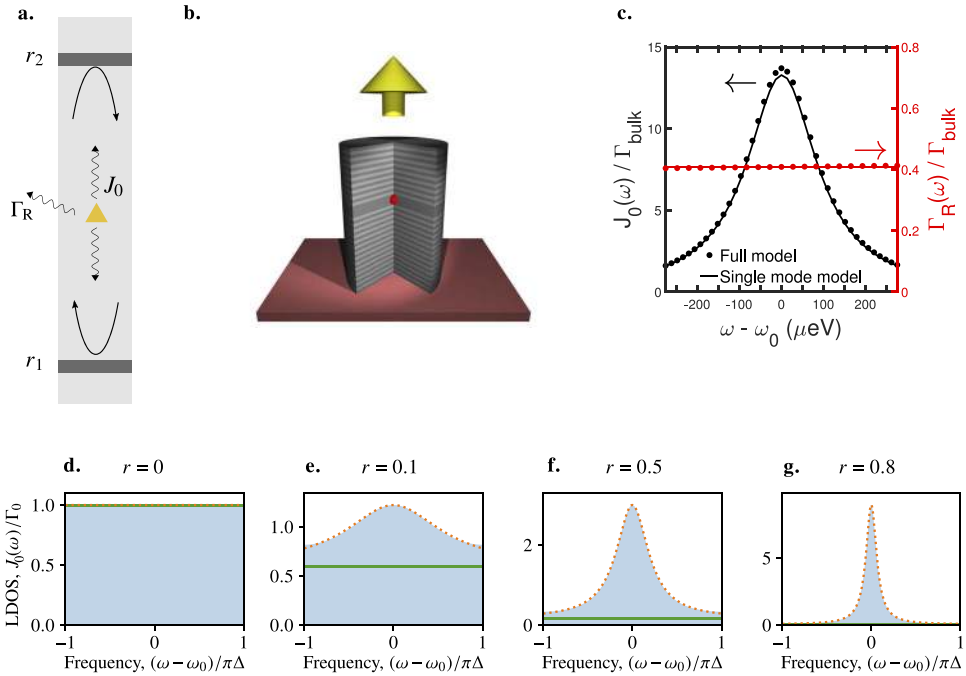

Fig. 2. a. Schematic of cavity model consisting of a waveguiding background medium with two mirrors. **b.** Artistic illustration of the micropillar single-photon source geometry. **c.** $J_0(\omega)$ (black) and $\Gamma_R(\omega)$ (red) computed using the full model (points) and the single-mode model, Eq. (5) (solid lines). Both are normalized to the LDOS of a bulk material, Γ_{bulk}. The pillar features 15 (25) DBR layer pairs in the top (bottom) mirror and a diameter of 2.5 μm, see Ref. [41] for further geometrical details. **d.–g.** Waveguide Γ_{WG} (green solid) and cavity (orange dotted, plotted as offset from green solid line) contributions to LDOS, where $\Delta = c/(\bar{n}L)$ is the free spectral range of the cavity. The LDOS from Eq. (5) is plotted with blue shading. Panels d-g correspond to mirror reflectivities of 0, 0.1, 0.5 and 0.8, respectively.

2.1. *Optical local density of states of a nanocavity*

The Hamiltonians describing the free evolution of the electromagnetic field and its interaction with the emitter are given by $H_F = \hbar \sum_\mu \omega_\mu a_\mu^\dagger a_\mu$, $H_{EF} = \hbar \sum_\mu (h_\mu a_\mu \sigma^\dagger + h_\mu^* a_\mu^\dagger \sigma)$. Here, $\sigma = |g\rangle\langle e|$ is the dipole operator of the emitter, a_μ and $a_\mu^\dagger$ are the bosonic annihilation and creation operators for the μ^{th} electric field mode with frequency ω_μ and coupling strength to the emitter h_μ. These coupling strengths depend both on the structure of the electromagnetic field and the position and orientation of the emitter, and are thus neither an intrinsic property of the field nor the emitter alone. A central object that characterises the emitter–field dynamics is the projected local density of states (LDOS) of the electromagnetic field in the optical structure, which is related to the optical field normal modes $\mathbf{u}_\mu(\mathbf{r}, \omega)$ as [35,36]

$$\mathcal{J}(\mathbf{r}, \omega, \mathbf{n}_p) = \sum_\mu \left[\mathbf{n}_p \cdot \left(\mathbf{u}_\mu(\mathbf{r}, \omega) \mathbf{u}_\mu^*(\mathbf{r}, \omega) \right) \cdot \mathbf{n}_p \right] \delta(\omega_\mu - \omega). \tag{2}$$

The projected LDOS depends on the frequency ω, the position $\mathbf{r}$ as well as the orientation $\mathbf{n}_p$ of the emitter dipole. The projected LDOS is related to the spectral density of the electric field in

Optical Materials EXPRESS

the light–matter interaction [35,36],

$$J(\mathbf{r},\omega,\mathbf{n}_\mathrm{p}) = \frac{\pi p^2 \omega}{\epsilon_0 \hbar}\mathcal{J}(\mathbf{r},\omega,\mathbf{n}_\mathrm{p}) = 2\pi \sum_\mu |h_\mu|^2 \delta(\omega-\omega_\mu), \tag{3}$$

where p is the dipole moment of the emitter. In the remainder of this paper, we assume that the QD is placed in a field antinode and skip the indices $\mathbf{r}$ and $\mathbf{n}_\mathrm{p}$ for simplicity, and furthermore we generally refer to J as defined in Eq. (3) as the LDOS or the spectral density of the field. In the weak light–matter coupling limit, $J(\omega)$ gives the spontaneous emission rate, when evaluated at the emitter frequency, ω_{eg}. In the strong coupling regime, one needs to identify a discrete cavity mode from the LDOS, in order to resolve coherent, reversible exchange of energy between the emitter and the field in the form of vacuum Rabi oscillations.

Exact calculations of the LDOS are numerically demanding, and the wide range of modes μ generally contributing to $J(\omega)$ complicates the analysis of the physics. However, if the QD is placed in a single-mode waveguide supporting only a single fundamental transverse mode in the frequency regime of interest, the LDOS can be well described using a single-mode model as the sum

$$J(\omega) = J_0(\omega) + \Gamma_\mathrm{R}(\omega), \tag{4}$$

where $J_0(\omega)$ and $\Gamma_\mathrm{R}(\omega)$ are the contributions from the fundamental mode and radiation modes, respectively. The contribution $\Gamma_\mathrm{R}(\omega)$ varies slowly and can be approximated to its value $\Gamma_\mathrm{R}(\omega_0)$ at the cavity resonance frequency ω_0, while $J_0(\omega)$ is given in a single-mode picture [37] as

$$J_0(\omega) = \Gamma_0 \Re\left\{\frac{[1+\tilde{r}_1(\omega)][1+\tilde{r}_2(\omega)]}{1-\tilde{r}_1(\omega)\tilde{r}_2(\omega)}\right\}. \tag{5}$$

Here, $\tilde{r}_i(\omega)$ is the frequency-dependent complex fundamental mode reflection coefficient of the i^{th} mirror, including the propagation phase from the QD to the mirror, and Γ_0 is the spontaneous emission rate into the fundamental mode for a uniform waveguide without mirrors. The model takes into account the dependence of the spatial position of the dipole emitter through the reflection coefficients and the position (and orientation) dependent $\Gamma_0(\mathbf{r},\omega,\mathbf{n}_\mathrm{p})$ and $\Gamma_\mathrm{R}(\mathbf{r},\omega,\mathbf{n}_\mathrm{p})$ [37]. As with Γ_R, we shall assume that Γ_0 does not vary appreciably over the frequency range of interest. In the following we assume an emitter placed in the center of the cavity and we write the complex reflection coefficients as $\tilde{r}_i(\omega) = r_i e^{i\phi_i + i\beta(\omega)L}$, with ϕ_i being the constant mirror reflection phase and $\beta(\omega) = \omega\bar{n}/c$ the dispersion-less propagation factor. The model, Eqs. (4)–(5), can be applied to a multi-mode waveguide either by including the contributions from higher-order guided modes to the LDOS explicitly [38] or by simply absorbing them into $\Gamma_\mathrm{R}(\omega)$.

An example of a single-photon source geometry well described by Eq. (5) is the multi-mode micropillar geometry illustrated in Fig. 2(b). Spectra for $J_0(\omega)$ and $\Gamma_\mathrm{R}(\omega)$ for the micropillar computed using the single-mode model Eq. (5) as well as from full numerical simulations are presented in Fig. 2(c). Excellent agreement between the single-mode model and the full simulation is observed, and the physics of the LDOS can thus be fully understood from the simple Eq. (5). Our model, Eqs. (4)–(5), can be applied to etalon-type structures, including photonic crystal waveguides [39], where modal reflection coefficients can be defined. However, for other classes of resonant modes, e.g. plasmonic resonances [40], the modal reflectivity may not be well-defined, and in this case, an alternative model based e.g. on a quasi-normal mode formulation [40] is required.

2.2. Waveguide and cavity contributions to the local density of states

If the reflectivity of the mirrors is sufficiently high, the LDOS $J_0(\omega)$ in the vicinity of a resonant frequency can be described by a Lorentzian function corresponding to a single damped cavity mode. However, as the system reduces to a photonic waveguide for vanishing reflectivity, there

Optical Materials EXPRESS

exists an intermediate reflectivity regime where the LDOS around a cavity resonance cannot be described by a single Lorentzian cavity mode, but also contains a flat background contribution, Γ_{WG} [38], as illustrated in Figs. 2(d)–2(g). When calculating the quantum dynamics and emission properties of the system, one is typically interested in the cavity quantum electrodynamical (cQED) parameters that characterise the optical structure: The cavity decay rate, κ, the cavity–emitter coupling strength, g, and the spontaneous emission rate into the underlying waveguide, Γ_{WG}. All of these properties can be derived from the LDOS, which is described by its corresponding microscopic parameters: The spontaneous emission rate into the bare waveguide, Γ_0, the mirror reflectivities, r_i, the effective index of the guided mode, $\bar{n}$, and the cavity length, L. The spontaneous emission rate into the bare waveguide, Γ_0, depends strongly on the structure of the waveguide. For example, a photonic crystal waveguide uses slow-light effects to enhance Γ_0 relative to the spontaneous emission into radiation modes, Γ_R [42–44]. The mapping between the microscopic and QED parameters can be performed by requiring that the effective spectral density generated by the QED system is equivalent to the optical LDOS [38,45]. In Fig. 3, we show how the QED parameters depend on the mirror reflectivity for three different cavity lengths and all other parameters kept constant. For vanishing mirror reflectivity, the emitter–cavity coupling strength approaches zero and the waveguide contribution to the LDOS, Γ_{WG}, approaches Γ_0, consistent with the fact that the optical structure simply becomes identical to the underlying waveguide. For increasing reflectivities, the waveguide component vanishes, and the coupling strength saturates at a value, which is proportional to $L^{-1/2}$. This scaling is essentially linked to the underlying proportionality $g \propto V^{-1/2}$. The cavity decay rate, κ, monotonically decreases with mirror reflectivity, as expected. Importantly, κ does not diverge as $r \to 0$, but reaches a finite value. This feature is attributed to causality, meaning that light cannot escape a finite spatial region infinitely fast.

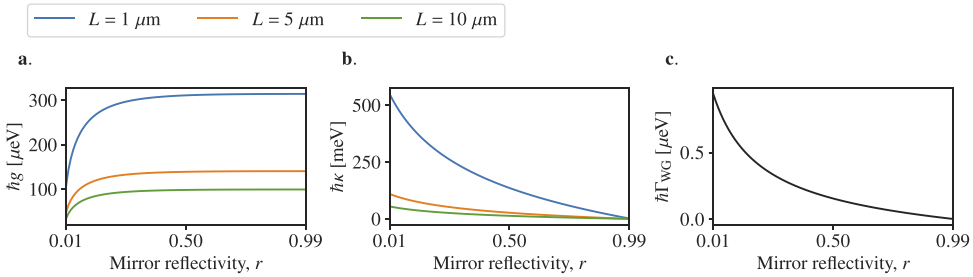

Fig. 3. a. Emitter–cavity coupling strength, **b.** cavity linewidth and **c** spontaneous emission rate into waveguide as a function of mirror reflectivity for a symmetric cavity, $r_1 = r_2 = r$. The blue, orange and green lines correspond to $L = 1$ μm, $L = 5$ μm and $L = 10$ μm, respectively. The spontaneous emission rate into the waveguide, Γ_{WG}, is independent of the cavity length. Parameters: $\bar{n} = 2$, $\hbar\Gamma_0 = 1$ μeV.

The approximation that the spontaneous emission rates into the fundamental waveguide mode and the radiation modes are frequency independent might not be fully justified for all parameter regimes of a given nanocavity structure. However, as discussed above, our analysis in the present paper qualitatively captures the behaviour of the important optical parameters as the properties of the underlying structure are varied.

3. Electron–phonon coupling and its signatures in the optical emission

State-of-the-art experiments have demonstrated that electron–phonon processes play a crucial role in determining the coherence properties of photons emitted from solid-state quantum emitters [23,46,47]. However, developing a theoretical model to accurately account for such processes

Optical Materials EXPRESS

remains a significant challenge. Phenomenological treatments typically assume a pure dephasing form for phonon dissipation, that is, an exponential suppression of the off-diagonal elements in the QD density operator [48]. This is only valid in very particular regimes [49] and misses key physics necessary to understand phonon processes, while also failing to capture key signatures of electron–phonon interactions, e.g. the presence of a phonon sideband.

In the following section we will outline how one may go beyond a simple pure dephasing treatment, introducing a microscopic model for electron–phonon processes in QDs. We will go on to discuss the polaron formalism, which allows one to capture complex non-perturbative effects—such as the phonon sideband—while maintaining a simple and intuitive dynamical description of the QD degrees of freedom.

3.1. Electron–phonon interactions in QDs

The dominant phonon coupling in self-assembled semiconductor QDs is to longitudinal acoustic (LA) phonons through a deformation potential coupling [50,51]. These phonons are natural oscillations of the host lattice, and can be approximated as a collection of harmonic oscillators. In the absence of electron-phonon coupling, the lattice dynamics are described by the free Hamiltonian $H_{\mathrm{P}} = \hbar \sum_{\mathbf{k}} \nu_{\mathbf{k}} \hat{b}^{\dagger}_{\mathbf{k}} \hat{b}_{\mathbf{k}}$, where $\nu_{\mathbf{k}}$ is the frequency of a phonon mode with wavevector $\mathbf{k}$, and $\hat{b}_{\mathbf{k}}$ ($\hat{b}^{\dagger}_{\mathbf{k}}$) is the corresponding annihilation (creation) operator.

When the charge configuration of the QD changes, for example, during the creation of an exciton, the lattice of the host material will reorganise itself in response. If the resulting displacement of the ions is small, the interaction between the emitter and the phonon environment is given by $H_{\mathrm{EP}} = |e\rangle\langle e|(V_{\mathrm{L}} + V_{\mathrm{Q}})$. This interaction consists of two terms corresponding to quite different phonon mechanisms: V_{L} gives rise to emission/absorption of a phonon wavepacket in the photon emission process, while V_{Q} describes virtual transitions to higher excitonic levels generated by thermal phonons (see Fig. 4(a)).

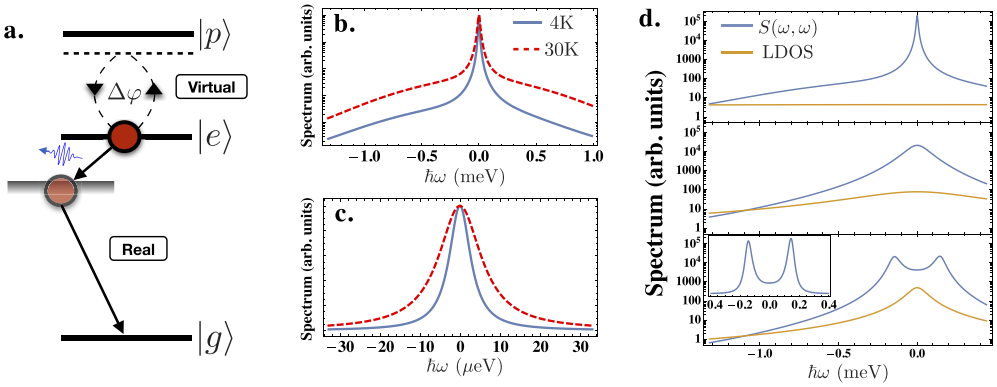

Fig. 4. **a.** Two phonon-induced processes affect the optical emission properties of QDs: Emission/absorption of phonon wavepacket during exciton relaxation and virtual transitions to higher-lying excitonic states through scattering of thermal phonons. **b.** Emission or absorption of a phonon wavepacket leads to a broad phonon sideband in the emission spectrum. **c.** Virtual scattering of thermal phonons leads to broadening of the zero-phonon line due to pure dephasing. **d.** When the QD is placed in an optical cavity, the electromagnetic LDOS influences the shape of the spectrum by funneling emission into the cavity resonance. In the strong coupling regime, the phonon scattering leads to an asymmetry between the polariton peaks [55].

Optical Materials EXPRESS

The first term is linear in phonon operators [52,53]:

$$V_{\mathrm{L}} = \sum_{\mathbf{k}} \hbar g_{\mathbf{k}} (b_{\mathbf{k}}^{\dagger} + b_{-\mathbf{k}}), \tag{6}$$

where $g_{\mathbf{k}}$ is the linear electron-phonon interaction strength for the $\mathbf{k}^{\mathrm{th}}$-phonon mode, and may be defined in terms of the phonon matrix elements $\hbar g_{\mathbf{k}} = \sum_{a=e,h} M_{a,\mathbf{k}}^{11}$, where for deformation potential coupling, the matrix element takes the form:

$$M_{a,\mathbf{k}}^{ij} = \sqrt{\frac{\hbar \nu_{\mathbf{k}}}{2\varrho c_s^2 \mathcal{V}}} D_a \int \psi_{i,a}^{*}(\mathbf{r}) \psi_{j,a}(\mathbf{r}) e^{i\mathbf{k}\cdot\mathbf{r}} \, \mathrm{d}^3 r, \tag{7}$$

reflecting phonon-induced transitions between the i^{th} and j^{th} electronic states. Here, we have introduced the quantisation volume $\mathcal{V}$ and the material parameters: the speed of sound c_s, material density ϱ, and the deformation potential for electrons D_e and holes D_h. The matrix element is also dependent on the wave function $\psi_{i,e/h}(\mathbf{r})$ of the confined electron (e) or hole (h). The linear phonon coupling describes real (energetically allowed) phonon processes, and can be interpreted as an exciton-induced displacement of the host lattice, as shown schematically in Fig. 1(a). This leads to the emergence of the phonon sideband in the emission spectrum (see Fig. 4(b) and a dephasing rate that depends on the emitter–cavity coupling strength, g.

The second term is quadratic in phonon operators, and takes the form [21–23]:

$$V_{\mathrm{Q}} = \sum_{\mathbf{k}\mathbf{k}'} \hbar f_{\mathbf{k},\mathbf{k}'} \left(b_{\mathbf{k}}^{\dagger} + b_{-\mathbf{k}}\right) \left(b_{\mathbf{k}'}^{\dagger} + b_{-\mathbf{k}'}\right), \tag{8}$$

describing phonon mediated virtual (energetically forbidden) transitions between the first exciton state and higher lying excited states, which have been eliminated perturbatively following Muljarov and Zimmerman [21]. These transitions are virtual in nature due to significant differences of energy scales. In a typical QD, the energy gap between the lowest excitonic state (s-shell) and the next state (p-shell) ~ 40 meV, is thus orders of magnitude greater than phonon energies at cryogenic temperatures [23]. With this in mind, we can intuitively understand the quadratic interaction term as virtual scattering of a phonon from mode $\mathbf{k}$ into $\mathbf{k}'$ mediated by the excitonic state, as shown schematically in Fig. 4(a). This scattering process imparts a random phase kick to the exciton, the cumulative effect of which is a temperature dependent broadening of the zero phonon line [54] (see Fig. 4(c)), which is absent when there is only a linear electron-phonon coupling term. The effective coupling strength for the quadratic coupling may be written in terms of the matrix elements $\hbar f_{\mathbf{k},\mathbf{k}'} = \sum_{a=e,h} \sum_{j>1} M_{a,\mathbf{k}}^{1j} M_{a,\mathbf{k}'}^{j1} [\hbar\omega_j^a - \hbar\omega_1^a]^{-1}$ and $\hbar\omega_j^{e/h}$ is the energy of the j^{th} electronic state.

3.2. Optical properties of a QD in a photonic environment

Calculating the dynamical and optical properties of a QD including phonon effects constitutes a challenging theoretical problem. Strong coupling between electronic and vibrational degrees of freedom means that standard perturbative treatments are insufficient, a fact that is compounded when the QD is interfaced with a complex photonic environment (e.g. a optical micropillar). In this section, we will outline the polaron formalism, which allows one to account for strong electron-phonon coupling in addition to strong coupling to complex photonic structures [55–57]. Numerically exact approaches based on real-time path integrals [58–61], non-equilibrium Green's functions [62] and diagonalisation of the Liouvillian [20,24,63,64] have previously been employed to solve similar problems. In contrast to these computationally demanding approaches, using perturbation theory in a polaron representation leads to numerically inexpensive implementations,

Optical Materials EXPRESS

and even allow analytical results in certain cases, while maintaining a high accuracy in the regimes relevant for single-photon sources.

We now consider the full Hamiltonian, Eq. (1), where the electromagnetic environment is described by a cavity mode with annihilation operator a, coupling strength g to the emitter, and decay rate κ, as described in Sec. 2.2.

First, a canonical transformation to the *polaron frame* generated by the unitary $\mathcal{U} = |g\rangle\langle g| + |e\rangle\langle e|e^{-S}$, with $S = \sum_{\mathbf{k}} \nu_{\mathbf{k}}^{-1} g_{\mathbf{k}}(b_{\mathbf{k}}^{\dagger} - b_{\mathbf{k}})$, is applied to total Hamiltonian. This transformation dresses the system with vibrational modes of the host material, removing the linear electron-phonon interaction term in the process, and provides an optimised basis for perturbation theory.

In the polaron frame we may derive a 2$^{\text{nd}}$-order master equation for the emitter and cavity mode which is non-perturbative in electron-phonon coupling strength, taking the form:

$$\dot{\rho}(t) = -i\left[H'_{\mathrm{E}}, \rho(t)\right] + \gamma\mathcal{D}_{\sigma^{\dagger}\sigma}[\rho(t)] + (\Gamma_{\mathrm{WG}} + \Gamma_{\mathrm{R}})\mathcal{D}_{\sigma}[\rho(t)] + \kappa\mathcal{D}_{a}[\rho(t)] + \mathcal{W}[\rho(t)], \tag{9}$$

where $\rho(t)$ is the reduced density operator of the QD and cavity mode, $\mathcal{D}_A[\rho(t)] = A\rho(t)A^{\dagger} - [A^{\dagger}A\rho(t) - \rho(t)A^{\dagger}A]/2$ the Lindblad superoperator, γ is the total pure-dephasing rate and $H'_{\mathrm{E}} = H_{\mathrm{E}} + gB(a\sigma^{\dagger} + a^{\dagger}\sigma)$ is the Hamiltonian describing the emitter and discrete cavity mode, where the coupling rate has been renormalised due to phonons by the factor B, which will be introduced shortly. The last term in Eq. (9),

$$\mathcal{W}[\rho(t)] = g^2\left\{[X, \rho(t)\Theta_X^{\dagger}] + [Y, \rho(t)\Theta_Y^{\dagger}] + \text{H.c.}\right\}, \tag{10}$$

is an additional phonon-induced dissipator. Here, we have defined the operators $X = \sigma^{\dagger}a + \sigma a^{\dagger}$ and $Y = i(\sigma^{\dagger}a - \sigma a^{\dagger})$ and $\Theta_q = \int_0^{\infty} \mathrm{d}\tau q(-\tau)\Lambda_q(\tau)$, with $q = X, Y$, $q(-\tau) = e^{-iH'_{\mathrm{E}}\tau}qe^{iH'_{\mathrm{E}}\tau}$, where Λ_q are the polaronic phonon correlation functions

$$\Lambda_X(\tau) = \frac{1}{2}B^2[e^{\varphi(\tau)} + e^{-\varphi(\tau)} - 2],\ \Lambda_Y(\tau) = \frac{1}{2}B^2[e^{\varphi(\tau)} - e^{-\varphi(\tau)}]. \tag{11}$$

The quantities B and $\phi(\tau)$ characterise the dynamical properties of the phonon environment and are given by $\varphi(\tau) = \sum_{\mathbf{k}} \nu_{\mathbf{k}}^{-2} g_{\mathbf{k}}^2(\cos(\nu_{\mathbf{k}}\tau)\coth(\hbar\nu_{\mathbf{k}}/2k_{\mathrm{B}}T) - i\sin(\nu_{\mathbf{k}}\tau))$ and $B = e^{-\phi(0)/2}$.

In the more general case, the background electromagnetic modes that give rise to Γ_{R} and Γ_{WG} can potentially have a spectral density that varies appreciably over the frequency range of the phonon sideband. In such cases, phonon interactions renormalise the resulting spontaneous emission rate [65].

The pure dephasing rate, γ, entering the master equation, contains contributions from charge/spin noise, γ_0, and thermal phonon scattering induced by virtual p-shell transitions, γ_{P} [22,23], such that $\gamma = \gamma_0 + \gamma_{\mathrm{P}}$. The form of the phonon-induced pure-dephasing rate will be introduced in the next section.

The master equation Eq. (9) can be written in the compact form $\dot{\rho}(t) = \mathcal{L}\rho(t)$, where $\mathcal{L}$ is the Liouvillian superoperator. The two-time correlation function of the emitter dipole can be numerically calculated using the Liouvillian as

$$\langle\sigma^{\dagger}(t+\tau)\sigma(t)\rangle \simeq G_{\mathrm{P}}(\tau)\mathrm{Tr}[\sigma^{\dagger}e^{\mathcal{L}\tau}\sigma e^{\mathcal{L}t}\rho(0)],\quad \tau, t > 0, \tag{12}$$

where $G_{\mathrm{P}}(\tau) = B^2e^{\varphi(\tau)}$ is the polaronic free-phonon correlation function that accounts for the transformation from the polaron frame to the natural 'lab frame'. The Fourier transformation of this correlation function gives the two-colour dipole spectrum, $S_0(\omega, \omega') = \int_{-\infty}^{\infty} \mathrm{d}t\mathrm{d}t' e^{i(\omega t - \omega' t')}\langle\sigma^{\dagger}(t)\sigma(t')\rangle$. However, since the QD is placed in an optical structure, the measurable quantity is not the bare dipole spectrum $S_0(\omega, \omega')$, but the spectrum of the electromagnetic field emitted from the structure. This field spectrum $S(\omega, \omega')$ is related to the dipole

Optical Materials EXPRESS

spectrum through an optical Green's function, G_{E}, as

$$S(\omega,\omega') = G_{\mathrm{E}}^{*}(\omega)G_{\mathrm{E}}(\omega')S_0(\omega,\omega') \tag{13}$$

where, up to an irrelevant phase factor, the Green's function is given by

$$G_{\mathrm{E}}(\omega) = \frac{[1+\tilde{r}_1(\omega)]t_2}{1-\tilde{r}_1(\omega)\tilde{r}_2(\omega)}, \tag{14}$$

and $t_i = \sqrt{1-r_i^2}$ is the mirror transmittivity [38]. This method of linking the dipole spectrum to the emission spectrum of the electric field through a Green's function is similar to the approach in Ref. [66]. We note that although Eq. (13) is nonperturbative in the light–matter coupling strength, the approach is only valid up to the onset of strong coupling, because the approximation in Eq. (12) breaks down. Furthermore, we note that in our analysis, it is assumed that the detected electric field is that carried by the fundamental waveguide mode outside the cavity region, whereby the detected field becomes independent of the position of the detector, up to an irrelevant phase factor. The approach can be extended to any general detection scenario by replacing G_{E} with an explicitly position-dependent Green's function that describes the propagation of emitted light to the detector. The two-colour spectrum, $S(\omega,\omega')$, is a generalisation of the power spectrum, $\bar{S}(\omega) = S(\omega,\omega)$. Moreover, it carries information about the coherence properties and thus allows for calculation of the photon indistinguishability, which in the absence of multi-photon emission reads [6,30,63]

$$\mathcal{I} = \left(\frac{\Gamma_0}{2P}\right)^2 \int_{-\infty}^{\infty} \mathrm{d}\omega \mathrm{d}\omega' |S(\omega,\omega')|^2. \tag{15}$$

Here, P is the total emitted energy into the optical structure during the relaxation of the initial QD exciton, $P = (\Gamma_0/2)\int_{-\infty}^{\infty}\mathrm{d}\omega S(\omega,\omega)$. Besides from the approximations associated with calculation of the two-colour spectrum, $S(\omega,\omega')$, Eq. (15) is an exact expression for the indistinguishability, derived from the Fourier transformation of the definition of $\mathcal{I}$ based on the Hong-Ou-Mandel correlation function [30]. The quantum efficiency of the source is then $\mathcal{E} = P/(P+P_{\mathrm{R}})$, where $P_{\mathrm{R}} = \Gamma_{\mathrm{R}}\int_{-\infty}^{\infty}\mathrm{d}\omega S_0(\omega,\omega)$ is the total energy emitted into the radiation modes.

To understand the spectral features of the emitted light, we may write the dipole power spectrum as $\bar{S}_0(\omega) = \bar{S}_0^{\mathrm{zpl}}(\omega) + \bar{S}_0^{\mathrm{psb}}(\omega)$, with two distinct spectral components that correspond to the zero-phonon line and the phonon sideband, respectively,

$$\bar{S}_0^{\mathrm{zpl}}(\omega) = B^2 \int_{-\infty}^{\infty} \mathrm{d}t\ \mathrm{d}\tau \langle \sigma^{\dagger}(t+\tau)\sigma(t)\rangle e^{i\omega\tau}, \tag{16}$$

$$\bar{S}_0^{\mathrm{psb}}(\omega) = \int_{-\infty}^{\infty} \mathrm{d}t\ \mathrm{d}\tau (G_{\mathrm{P}}(\tau) - B^2)\langle \sigma^{\dagger}(t+\tau)\sigma(t)\rangle e^{i\omega\tau}. \tag{17}$$

The first contribution, $\bar{S}_0^{\mathrm{zpl}}$, describes the spectral features arising from photon emission without emitting any phonons. The prefactor, B^2, to this contribution is the Frank-Condon (FC) factor, $0 < B < 1$, which quantifies the fraction of light emitted into the zero-phonon line [67].

The second contribution, $\bar{S}_0^{\mathrm{psb}}$, describes photons emitted while a phonon wavepacket is absorbed or emitted. This spectral component emerges through the linear electron–phonon coupling. Since the temporal features of the phonon correlation function, $G_{\mathrm{P}}(\tau)$, are very fast, on the order of a few ps, the spectral features of $\bar{S}_0^{\mathrm{psb}}$ are very broad – on the order of a few meV.

3.3. Electron-phonon coupling parameters

In order to calculate the influence of phonons on the optical properties of a QD, it is necessary to specify the linear and quadratic electron-phonon coupling strengths. To do so, it is clear

Optical Materials EXPRESS

from Eq. (7) that we must first specify the wave function of electrons and holes confined within the QD. However, calculating exciton wave functions for realistic QDs is a highly non-trivial task, requiring sophisticated and expensive computational methods [68–70]. Instead, we can accurately reproduce both the qualitative and quantitative effects of phonons by considering an idealised model for a QD. Here we assume the QD confinement to be parabolic, spherically symmetric, and the electrons and holes have the same confinement length [53,64]. Relaxing such approximations leads to the emergence of complex phonon behaviour, including the quenching of phonon modes for specific asymmetries between the electron-hole confinement potentials [71].

Using the above approximations we may obtain analytic forms for the polaron frame propagator [55,57] $\varphi(\tau) = \alpha \int_0^\infty \nu e^{-\nu^2/\nu_c^2}(\cos(\nu\tau)\coth(\hbar\nu/2k_BT) - i\sin(\nu\tau))$, where we have taken a continuum limit over the phonon modes assuming a linear dispersion relation. We have also introduced the electron-phonon coupling strength, which may be written in terms of material parameters $\alpha = [4\pi^2\hbar\varrho c_s^5]^{-1}(D_e - D_h)^2$. Using typical material parameters for GaAs QDs (see Table 1), we find $\alpha = 0.025$ ps^2. The electron-phonon interaction strength is also determined by the cut-off frequency $\nu_c = \sqrt{2}c_s/d$, where d is the confinement length of the QD.

With the electron-phonon coupling fully characterised, it is worth briefly considering the regime of validity of the polaron master equation described in Sec. 3.2. The polaron transformation results in a master equation that incorporates electron-phonon coupling to all orders, with the light-matter coupling strength becoming the relevant perturbative parameter in the transformed frame. Following McCutcheon and Nazir [57], the resulting master equation can be found to be valid in regimes where $(2g/\nu_c)^2(1 - B^4) << 1$.

If we assume that the dominant contribution to the quadratic phonon-interaction arises from virtual transition between the first and second excited states of the QD (i.e. the s- and p-shells), then we may also find an analytic form for the pure dephasing rate [22,23]:

$$\gamma_P = \frac{\alpha\mu}{\nu_c^4}\int_0^\infty \nu^{10}e^{-2\nu^2/\nu_c^2}n(\nu)(n(\nu)+1)d\nu, \tag{18}$$

where $n(\nu) = [\exp(\hbar\nu/k_BT) - 1]^{-1}$ is the bosonic occupation number and $\mu = \hbar^2\pi[D_e - D_h]^{-4}(\Delta_e^{-1}D_e^2 + \Delta_h^{-1}D_h^2)^2$, where $\Delta_{e/h}$ is the energy difference between the s- and p-states for the electron/hole, and naturally depends on the confinement potential of the QD. For a spherically symmetric, harmonic potential, it is simply given by $\Delta_{e/h} = \hbar^2/(d^2m_{e/h})$, where $m_{e/h}$ is the effective electron/hole mass.

Both the FC factor and the pure dephasing rate are dependent on temperature. In the case of the FC factor, as temperature increases, B decreases due to an increasing fraction of light being emitted by the phonon sideband rather than by the ZPL. The pure dephasing rate, on the other hand, increases, as more phonons are available to drive virtual transitions between the electronic states. Crucially this dephasing rate freezes out at low temperatures owing to the quadratic dependence of the rate on the phonon occupation, physically this corresponds to an absence of phonons in the environment available to drive transitions.

Table 3.3 shows realistic parameters for GaAs QDs, which are generally used for calculations in this paper unless otherwise stated [72,73].

Table 1. Material parameters for GaAs [72,73] used for calculation of electron–phonon coupling parameters. m_0 denotes the free electron mass.

D_e [meV]	D_h [meV]	ϱ [g/cm^3]	c_s [m/s]	m_e [m_0]	m_h [m_0]
−15.93	−8.77	5.317	4.73×10^3	0.067	0.51

Optical Materials EXPRESS

4. Phonon-induced limitations to single-photon sources

Due to the presence of the phonon sideband in the emission spectrum, a quantum dot–based single photon source cannot simultaneously have unity efficiency and indistinguishability [67]: If the emission spectrum is left unfiltered, the indistinguishability is reduced below unity due to the photons in the sideband, which are uncorrelated with those of the zero-phonon line that have not undergone phonon scattering. On the other hand, while filtering out the sideband revives the indistinguishability, it comes with the cost of a reduction in efficiency, corresponding to the fraction of photons contained in the sideband. By placing the emitter in a photonic cavity with a narrow resonance line, the emission can be preferentially funneled into the zero-phonon line via the Purcell effect, thereby simultaneously improving the indistinguishability and efficiency. However, this strategy only continues to improve the performance as long as the emitter–cavity system is in the Purcell regime. As soon as the system enters the strong coupling regime, where the cavity lifetime is long enough for the emitter to re-absorb an emitted photon and the system undergoes vacuum Rabi oscillations, the phonon environment will drive incoherent transitions from the upper polariton state to the lower one [63]. This polaritonic relaxation process drastically degrades the coherence of the emitted light and in turn sets the upper limit for the performance, as illustrated in Fig. 5, which shows the indistinguishability, efficiency and their product as a function of cavity linewidth (blue solid lines).

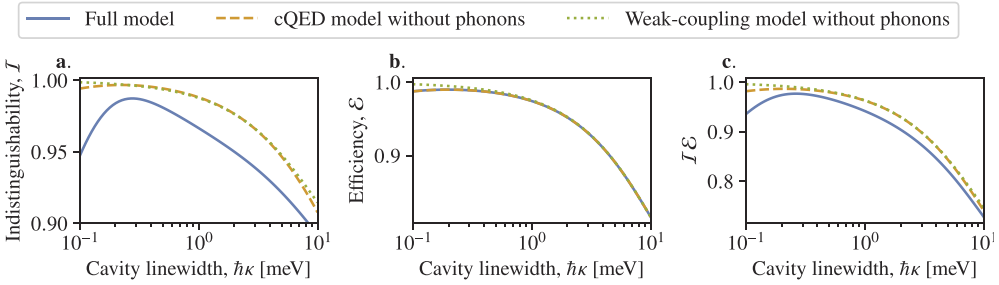

Fig. 5. a. Indistinguishability, $\mathcal{I}$ **b.** efficiency, $\mathcal{E}$, and **c.** their product, $\mathcal{I}\mathcal{E}$ as a function of cavity linewidth. Parameters: $\hbar\Gamma_0 = 1\ \mu$eV, $\hbar\Gamma_R = 1\ \mu$eV, $\hbar\gamma_0 = 0.5\ \mu$eV, $\hbar g = 100\ \mu$eV, $T = 4$ K and QD size $d = 10$ nm.

In recent reports on broadband ($\hbar\kappa \sim 10$ meV) sources of quantum light based on circular Bragg gratings, the measured indistinguishabilities of 0.90 [4] and 0.95 [5] are higher than that predicted in Fig. 5(a). However, here 150 GHz [4] and 5 GHz [5] etalons were used, leading to improved indistinguishability at the cost of efficiency as discussed above. While the indistinguishability measured in the absence of a filter is the relevant figure of merit describing the device performance in the context of scalable optical quantum information technology, it is only rarely [3] reported.

In the weak light–matter coupling regime, the indistinguishability and effiency can be approximated by the analytical expressions [6,38]

$$\begin{aligned}\mathcal{I} &= \frac{\Gamma_{\text{tot}}}{\Gamma_{\text{tot}}+\gamma_{\text{tot}}}\Big[\frac{(\Gamma_{\text{WG}}+\Gamma_{\text{cav}})B^2}{(\Gamma_{\text{WG}}+\Gamma_{\text{cav}})B^2+2\Gamma_0 F(1-B^2)}\Big]^2\\ \mathcal{E} &= \frac{(\Gamma_{\text{cav}}+\Gamma_{\text{WG}})B^2+2\Gamma_0 F(1-B^2)}{(\Gamma_{\text{cav}}+\Gamma_{\text{WG}})B^2+2\Gamma_0 F(1-B^2)+\Gamma_R},\end{aligned} \tag{19}$$

where F is the fraction of the phonon sideband that remains unfiltered by the cavity, $\Gamma_{\text{tot}} = \Gamma_{\text{cav}} + \Gamma_{\text{WG}} + \Gamma_R$ is the total population decay rate, $\Gamma_{\text{cav}} = 4g^2/\kappa$ is the Purcell-enhanced emission rate into the cavity and $\gamma_{\text{tot}} = \gamma + 4\pi(gB/\kappa)^2\alpha(2gB)^2 e^{-(2gB/\nu_c)^2}\coth[\hbar gB/(k_B T)]$ is the total

Optical Materials EXPRESS

dephasing rate, accounting for pure dephasing and additional phonon-induced dephasing due to scattering between the cavity–exciton polaritons.

If one assumes that the emitter–cavity coupling is weak and that phonon effects can be described by a constant pure dephasing rate, γ, one ends up with a simple model leading to the result [27]

$$\mathcal{I} = \frac{\Gamma_{\text{tot}}}{\Gamma_{\text{tot}} + \gamma}, \quad \mathcal{E} = \frac{\Gamma_{\text{cav}} + \Gamma_{\text{WG}}}{\Gamma_{\text{tot}}}. \tag{20}$$

These expressions for $\mathcal{I}$ and $\mathcal{E}$ are indicated with dotted green lines in Fig. 5. According to Eq. (20), the performance will monotonically improve as the cavity Q-factor is increased, due to the Purcell effect. However, the theory fails to reproduce the correct qualitative and quantitative behaviour of the efficiency and in particular the indistinguishability. This discrepancy is due to the neglect of the phonon sideband in the simple model, and due to the fact that Eq. (20) is not valid in the strong-coupling regime. To illustrate this, we also report the indistinguishability and efficiency predicted by a cavity QED model that fully accounts for strong coupling but does not include phonons, as in Refs. [27,48,74,75] (dashed orange lines). The discrepancy between the phonon-less cQED model and the weak-coupling Purcell-approximation does not arise due to strong coupling itself, but rather due to the interplay between strong coupling, pure dephasing and losses. In the strong coupling regime, pure dephasing and losses have a larger impact than predicted by the weak coupling approximation because the initial excitation of the emitter does not monotonically decay into the cavity and leaks out, but returns to the emitter in each vacuum Rabi cycle.

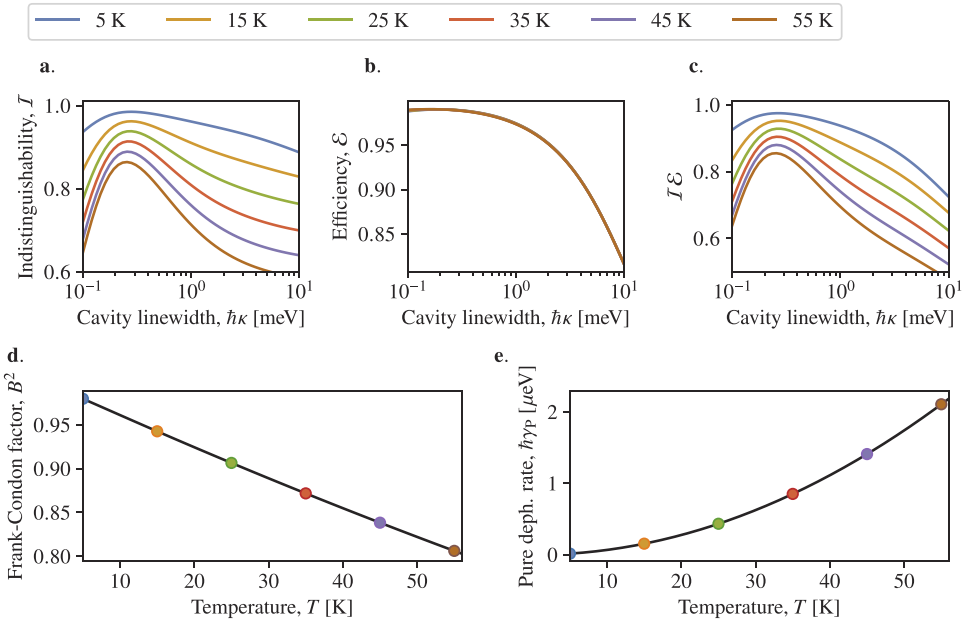

Fig. 6. a. Indistinguishability, $\mathcal{I}$ **b.** efficiency, $\mathcal{E}$, and **c.** their product, $\mathcal{I}\mathcal{E}$ as a function of cavity linewidth, where the blue lines correspond to a temperature of 5 K, the brown lines to 55 K and the remaining lines spaced regularly in steps of 10 K. **d.** Frank-Condon factor, B^2, as a function of temperature, with coloured circles indicating the temperatures of the corresponding coloured lines in panels a-c. **e.** Phonon-induced pure dephasing rate of the zero-phonon line as a function of temperature. As for panel e, the coloured circles correspond to the coloured lines in panels a-c. Parameters: $\hbar\Gamma_0 = 1$ μeV, $\hbar\Gamma_R = 1$ μeV, $\hbar\gamma_0 = 0.5$ μeV, $\hbar g = 100$ μeV and QD size $d = 10$ nm.

Optical Materials EXPRESS

A typical experimental strategy for tuning the emitter into resonance with an optical cavity is to change the temperature [2]. Figures 6(a)–6(c) presents the single-photon source performance as a function of cavity linewidth for temperatures in the range 5 – 55 K. With increased temperature, the thermal phonon population will enhance the fraction of emission into the phonon sideband ($1 - B^2$) and increase the phonon-induced pure dephasing rate [23,25]. These two effects are quantified in Figs. 6(d)–6(e), with coloured circles indicating the temperature of the corresponding lines in Fig. 6(a)–6(c).

The size of the QD also has a strong impact on the emission properties. This is illustrated in Fig. 7, where the indistinguishability, efficiency and their product is shown for a range of QD sizes, d. The QD size has an impact on the FC factor, the energy splitting between the excitonic states and the phonon cutoff-frequency. The FC factor increases monotonically with QD size, because the cutoff-frequency is inversely proportional with the size. This means that for larger QDs, the power in the sideband is decreased relative to the zero-phonon line. The splitting between the s- and p-shell excitons scales as d^{-2}. For this reason, the rate of pure dephasing induced by virtual scattering of thermal phonons increases as the QD becomes larger, but only for relatively small QDs. As seen in Eq. (18), the pure-dephasing rate involves a frequency integral over $e^{-(\nu/\nu_c)^2}$. As the size is increased, the cutoff-frequency, ν_c, will decrease as d^{-1}, and thus eventually the pure dephasing rate will decrease with increasing size. It is worth mentioning that these calculations have been performed under the assumption of a spherically symmetric QD, and more intricate features might be revealed when the confinement potential mimicks the shape of a realistic QD more closely. Furthermore, we have taken the spontaneous emission rates, Γ_0 and Γ_R, to be independent of the QD size. Strictly speaking, these rates are size-dependent,

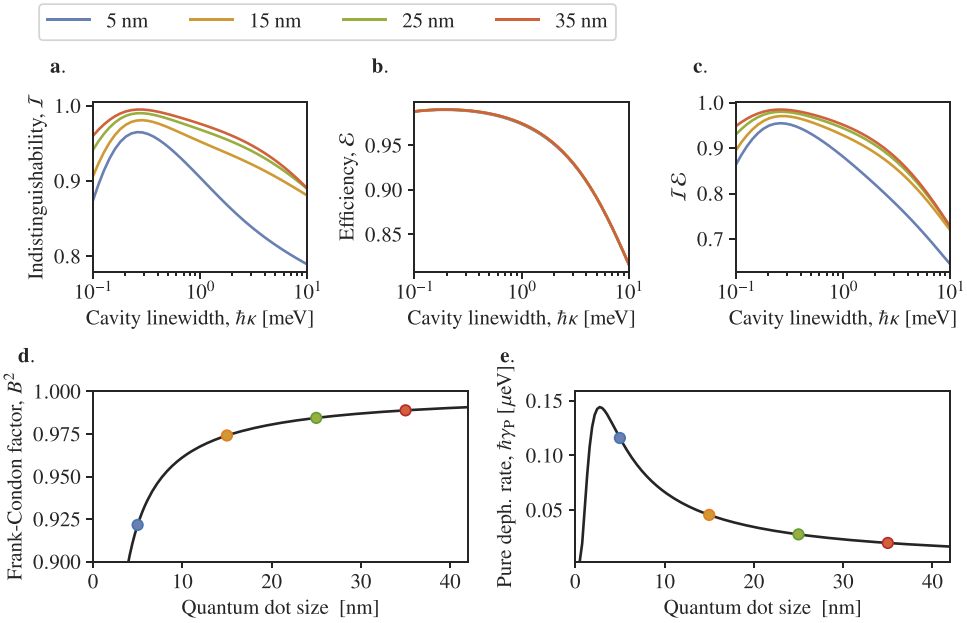

Fig. 7. a. Indistinguishability, $\mathcal{I}$ **b.** efficiency, $\mathcal{E}$, and **c.** their product, $\mathcal{I}\mathcal{E}$ as a function of cavity linewidth, where each line corresponds to a different QD size **d.** Frank-Condon factor, B^2, as a function of QD size, with coloured circles indicating the temperatures of the corresponding coloured lines in panels a-c. **e.** Phonon-induced pure dephasing rate of the zero-phonon line as a function of QD size. As for panel e, the coloured circles correspond to the coloured lines in panels a-c. Parameters: $\hbar\Gamma_0 = 1$ μeV, $\hbar\Gamma_R = 1$ μeV, $\hbar\gamma_0 = 0.5$ μeV, $\hbar g = 100$ μeV, $T = 10$ K.

Optical Materials EXPRESS

although experiments have shown a very modest variation over the sizes used here [76]. We do, however, note that care should be taken when going to the large-dot limit, where the light-matter interaction may be strongly influenced by the QD size [77–79].

5. Outlook

Although this article focuses on intrinsic limitations of quantum dots as single-photon sources, quantum dots remain among the most promising solid-state emitters for on-demand high-rate generation of single photons with simultaneous high efficiency and indistinguishability. In comparison to other leading solid-state quantum emitters, the electron-phonon interaction strength of QDs is relatively weak, with $\sim 90\%$ of light emitted through the zero phonon line in bulk at cryogenic temperatures. For example, in contrast, Nitrogen Vacancy centers diamond emit only $\sim 3\%$ of photons through the zero phonon line [80], while displaying better spin coherence properties than quantum dots. Furthermore, the natural integrability of QDs in photonic structures allows to engineer emission properties and may vastly improve the coherence of emitted photons.

Many important properties of quantum dots and their interaction with a photonic environment remain to be answered. Recent studies investigate the dynamics and limitations of the optical excitation process [10] and demonstrate how the phonon sideband can be used to increase the pumping efficiency without sacrificing the photon indistinguishability [11]. Other recent investigations focus on the properties of light scattered from a solid-state quantum emitter [81,82]. Furthermore, a larger parameter space and a range of new phenomena arise when the Fabry-Perot cavity is replaced with a non-Lorenzian cavity, which opens up a rich class of dynamics [83,84]. We also note that the topic of phonon effects in quantum dots has recently been reviewed with focus on optical excitation schemes [85] and in a broader scope, presenting a range of different phonon-induced phenomena and theoretical modeling techniques [86].

Funding

Det Frie Forskningsråd (DFF-4181-00416); Royal Commission for the Exhibition of 1851; Villum Fonden (8692); QuantERA ERA-NET Cofund (HYPER-U-P-S).

Disclosures

The authors declare no conflicts of interest.

References

1. J. L. O'Brien, "Optical Quantum Computing," Science **318**(5856), 1567–1570 (2007).
2. X. Ding, Y. He, Z.-C. Duan, N. Gregersen, M.-C. Chen, S. Unsleber, S. Maier, C. Schneider, M. Kamp, S. Höfling, C.-Y. Lu, and J.-W. Pan, "On-demand single photons with high extraction efficiency and near-unity indistinguishability from a resonantly driven quantum dot in a micropillar," Phys. Rev. Lett. **116**(2), 020401 (2016).
3. N. Somaschi, V. Giesz, L. De Santis, J. C. Loredo, M. P. Almeida, G. Hornecker, S. L. Portalupi, T. Grange, C. Antón, J. Demory, C. Gómez, I. Sagnes, N. D. Lanzillotti-Kimura, A. Lemaître, A. Auffeves, A. G. White, L. Lanco, and P. Senellart, "Near-optimal single-photon sources in the solid state," Nat. Photonics **10**(5), 340–345 (2016).
4. J. Liu, R. Su, Y. Wei, B. Yao, S. F. C. da Silva, Y. Yu, J. Iles-Smith, K. Srinivasan, A. Rastelli, J. Li, and X. Wang, "A solid-state source of strongly entangled photon pairs with high brightness and indistinguishability," Nat. Nanotechnol. **14**(6), 586–593 (2019).
5. H. Wang, Y.-M. He, T.-H. Chung, H. Hu, Y. Yu, S. Chen, X. Ding, M.-C. Chen, J. Qin, X. Yang, R.-Z. Liu, Z.-C. Duan, J.-P. Li, S. Gerhardt, K. Winkler, J. Jurkat, L.-J. Wang, N. Gregersen, Y.-H. Huo, Q. Dai, S. Yu, S. Höfling, C.-Y. Lu, and J.-W. Pan, "Towards optimal single-photon sources from polarized microcavities," Nat. Photonics **13**(11), 770–775 (2019).
6. J. Iles-Smith, D. P. S. McCutcheon, A. Nazir, and J. Mørk, "Phonon scattering inhibits simultaneous near-unity efficiency and indistinguishability in semiconductor single-photon sources," Nat. Photonics **11**(8), 521–526 (2017).
7. N. Gregersen, P. Kaer, and J. Mørk, "Modeling and design of high-efficiency single-photon sources," IEEE J. Sel. Top. Quantum Electron. **19**(5), 1–16 (2013).
8. R. H. Brown and R. Q. Twiss, "Correlation between photons in two coherent beams of light," Nature **177**(4497), 27–29 (1956).

Optical Materials EXPRESS

9. K. A. Fischer, L. Hanschke, J. Wierzbowski, T. Simmet, C. Dory, J. J. Finley, J. Vučković, and K. Müller, "Signatures of two-photon pulses from a quantum two-level system," Nat. Phys. **13**(7), 649–654 (2017).
10. C. Gustin and S. Hughes, "Pulsed excitation dynamics in quantum-dot–cavity systems: Limits to optimizing the fidelity of on-demand single-photon sources," Phys. Rev. B **98**(4), 045309 (2018).
11. C. Gustin and S. Hughes, "Efficient pulse-excitation techniques for single photon sources from quantum dots in optical cavities," Adv. Quantum Technol. p. 1900073 (2019).
12. C.-K. Hong, Z.-Y. Ou, and L. Mandel, "Measurement of subpicosecond time intervals between two photons by interference," Phys. Rev. Lett. **59**(18), 2044–2046 (1987).
13. E. Knill, R. Laflamme, and G. J. Milburn, "A scheme for efficient quantum computation with linear optics," Nature **409**(6816), 46–52 (2001).
14. E. Moreau, I. Robert, L. Manin, V. Thierry-Mieg, J. Gérard, and I. Abram, "Quantum cascade of photons in semiconductor quantum dots," Phys. Rev. Lett. **87**(18), 183601 (2001).
15. N. Akopian, N. Lindner, E. Poem, Y. Berlatzky, J. Avron, D. Gershoni, B. Gerardot, and P. Petroff, "Entangled photon pairs from semiconductor quantum dots," Phys. Rev. Lett. **96**(13), 130501 (2006).
16. A. Dousse, J. Suffczyński, A. Beveratos, O. Krebs, A. Lemaître, I. Sagnes, J. Bloch, P. Voisin, and P. Senellart, "Ultrabright source of entangled photon pairs," Nature **466**(7303), 217–220 (2010).
17. L. Besombes, K. Kheng, L. Marsal, and H. Mariette, "Acoustic phonon broadening mechanism in single quantum dot emission," Phys. Rev. B **63**(15), 155307 (2001).
18. B. Krummheuer, V. M. Axt, and T. Kuhn, "Theory of pure dephasing and the resulting absorption line shape in semiconductor quantum dots," Phys. Rev. B **65**(19), 195313 (2002).
19. I. Favero, G. Cassabois, R. Ferreira, D. Darson, C. Voisin, J. Tignon, C. Delalande, G. Bastard, P. Roussignol, and J. M. Gérard, "Acoustic phonon sidebands in the emission line of single InAs/GaAs quantum dots," Phys. Rev. B **68**(23), 233301 (2003).
20. P. Kaer and J. Mørk, "Decoherence in semiconductor cavity QED systems due to phonon couplings," Phys. Rev. B **90**(3), 035312 (2014).
21. E. A. Muljarov and R. Zimmermann, "Dephasing in quantum dots: Quadratic coupling to acoustic phonons," Phys. Rev. Lett. **93**(23), 237401 (2004).
22. P. Tighineanu, C. L. Dreessen, C. Flindt, P. Lodahl, and A. S. Sørensen, "Phonon decoherence of quantum dots in photonic structures: Broadening of the zero-phonon line and the role of dimensionality," Phys. Rev. Lett. **120**(25), 257401 (2018).
23. A. Reigue, J. Iles-Smith, F. Lux, L. Monniello, M. Bernard, F. Margaillan, A. Lemaître, A. Martinez, D. P. S. Mccutcheon, J. Mørk, R. Hostein, and V. Voliotis, "Probing electron-phonon interaction through two-photon interference in resonantly driven semiconductor quantum dots," Phys. Rev. Lett. **118**(23), 233602 (2017).
24. P. Kaer, N. Gregersen, and J. Mork, "The role of phonon scattering in the indistinguishability of photons emitted from semiconductor cavity QED systems," New J. Phys. **15**(3), 035027 (2013).
25. A. Thoma, P. Schnauber, M. Gschrey, M. Seifried, J. Wolters, J.-H. Schulze, A. Strittmatter, S. Rodt, A. Carmele, A. Knorr, T. Heindel, and S. Reitzenstein, "Exploring dephasing of a solid-state quantum emitter via time- and temperature-dependent hong-ou-mandel experiments," Phys. Rev. Lett. **116**(3), 033601 (2016).
26. A. V. Kuhlmann, J. Houel, A. Ludwig, L. Greuter, D. Reuter, A. D. Wieck, M. Poggio, and R. J. Warburton, "Charge noise and spin noise in a semiconductor quantum device," Nat. Phys. **9**(9), 570–575 (2013).
27. P. Senellart, G. Solomon, and A. White, "High-performance semiconductor quantum-dot single-photon sources," Nat. Nanotechnol. **12**(11), 1026–1039 (2017).
28. R. N. Malein, T. S. Santana, J. M. Zajac, A. C. Dada, E. Gauger, P. M. Petroff, J. Y. Lim, J. D. Song, and B. D. Gerardot, "Screening nuclear field fluctuations in quantum dots for indistinguishable photon generation," Phys. Rev. Lett. **116**(25), 257401 (2016).
29. B. Kambs and C. Becher, "Limitations on the indistinguishability of photons from remote solid state sources," New J. Phys. **20**(11), 115003 (2018).
30. A. Kiraz, M. Atatüre, and A. Imamoğlu, "Quantum-dot single-photon sources: Prospects for applications in linear optics quantum-information processing," Phys. Rev. A **69**(3), 032305 (2004).
31. A. J. Bennett, D. C. Unitt, A. J. Shields, P. Atkinson, and D. A. Ritchie, "Influence of exciton dynamics on the interference of two photons from a microcavity single-photon source," Opt. Express **13**(20), 7772–7778 (2005).
32. S. Ates, S. M. Ulrich, S. Reitzenstein, A. Löffler, A. Forchel, and P. Michler, "Post-selected indistinguishable photons from the resonance fluorescence of a single quantum dot in a microcavity," Phys. Rev. Lett. **103**(16), 167402 (2009).
33. Y.-M. He, Y. He, Y.-J. Wei, D. Wu, M. Atatüre, C. Schneider, S. Höfling, M. Kamp, C.-Y. Lu, and J.-W. Pan, "On-demand semiconductor single-photon source with near-unity indistinguishability," Nat. Nanotechnol. **8**(3), 213–217 (2013).
34. T. Huber, A. Predojević, D. Föger, G. Solomon, and G. Weihs, "Optimal excitation conditions for indistinguishable photons from quantum dots," New J. Phys. **17**(12), 123025 (2015).
35. L. Novotny and B. Hecht, *Principles of Nano-optics* (Cambridge University Press, 2012).
36. P. Lodahl, S. Mahmoodian, and S. Stobbe, "Interfacing single photons and single quantum dots with photonic nanostructures," Rev. Mod. Phys. **87**(2), 347–400 (2015).
37. N. Gregersen, D. P. S. McCutcheon, J. Mørk, J.-M. Gérard, and J. Claudon, "A broadband tapered nanocavity for efficient nonclassical light emission," Opt. Express **24**(18), 20904–20924 (2016).

Optical Materials EXPRESS

38. E. V. Denning, J. Iles-Smith, A. D. Osterkryger, N. Gregersen, and J. Mork, "Cavity-waveguide interplay in optical resonators and its role in optimal single-photon sources," Phys. Rev. B **98**(12), 121306 (2018).
39. P. Lalanne, C. Sauvan, and J. P. Hugonin, "Photon confinement in photonic crystal nanocavities," Laser Photonics Rev. **2**(6), 514–526 (2008).
40. R.-C. Ge, P. T. Kristensen, J. F. Young, and S. Hughes, "Quasinormal mode approach to modelling light-emission and propagation in nanoplasmonics," New J. Phys. **16**(11), 113048 (2014).
41. P. Lalanne, J. P. Hugonin, and J. M. Gérard, "Electromagnetic study of the quality factor of pillar microcavities in the small diameter limit," Appl. Phys. Lett. **84**(23), 4726–4728 (2004).
42. V. M. Rao and S. Hughes, "Single quantum-dot purcell factor and β factor in a photonic crystal waveguide," Phys. Rev. B **75**(20), 205437 (2007).
43. V. M. Rao and S. Hughes, "Single quantum dot spontaneous emission in a finite-size photonic crystal waveguide: proposal for an efficient "on chip" single photon gun," Phys. Rev. Lett. **99**(19), 193901 (2007).
44. G. Lecamp, P. Lalanne, and J. Hugonin, "Very large spontaneous-emission β factors in photonic-crystal waveguides," Phys. Rev. Lett. **99**(2), 023902 (2007).
45. D. Tamascelli, A. Smirne, S. F. Huelga, and M. B. Plenio, "Nonperturbative treatment of non-Markovian dynamics of open quantum systems," Phys. Rev. Lett. **120**(3), 030402 (2018).
46. T. Grange, N. Somaschi, C. Antón, L. De Santis, G. Coppola, V. Giesz, A. Lemaître, I. Sagnes, A. Auffèves, and P. Senellart, "Reducing phonon-induced decoherence in solid-state single-photon sources with cavity quantum electrodynamics," Phys. Rev. Lett. **118**(25), 253602 (2017).
47. S. Gerhardt, J. Iles-Smith, D. P. S. McCutcheon, Y.-M. He, S. Unsleber, S. Betzold, N. Gregersen, J. Mørk, S. Höfling, and C. Schneider, "Intrinsic and environmental effects on the interference properties of a high-performance quantum dot single-photon source," Phys. Rev. B **97**(19), 195432 (2018).
48. T. Grange, G. Hornecker, D. Hunger, J.-P. Poizat, J.-M. Gérard, P. Senellart, and A. Auffèves, "Cavity-funneled generation of indistinguishable single photons from strongly dissipative quantum emitters," Phys. Rev. Lett. **114**(19), 193601 (2015).
49. D. P. S. McCutcheon and A. Nazir, "Model of the optical emission of a driven semiconductor quantum dot: Phonon-enhanced coherent scattering and off-resonant sideband narrowing," Phys. Rev. Lett. **110**(21), 217401 (2013).
50. J. Förstner, C. Weber, J. Danckwerts, and A. Knorr, "Phonon-assisted damping of Rabi oscillations in semiconductor quantum dots," Phys. Rev. Lett. **91**(12), 127401 (2003).
51. A. J. Ramsay, A. V. Gopal, E. M. Gauger, A. Nazir, B. W. Lovett, A. M. Fox, and M. S. Skolnick, "Damping of exciton Rabi rotations by acoustic phonons in optically excited InGaAs/GaAs quantum dots," Phys. Rev. Lett. **104**(1), 017402 (2010).
52. G. D. Mahan, *Many-Particle Physics* (Springer, US, 2000).
53. A. Nazir and D. P. S. McCutcheon, "Modelling exciton–phonon interactions in optically driven quantum dots," J. Phys.: Condens. Matter **28**(10), 103002 (2016).
54. M. Bayer and A. Forchel, "Temperature dependence of the exciton homogeneous linewidth in in 0.60 Ga 0.40 As/GaAs self-assembled quantum dots," Phys. Rev. B **65**(4), 041308 (2002).
55. I. Wilson-Rae and A. Imamoğlu, "Quantum dot cavity-QED in the presence of strong electron-phonon interactions," Phys. Rev. B **65**(23), 235311 (2002).
56. C. Roy and S. Hughes, "Phonon-dressed mollow triplet in the regime of cavity quantum electrodynamics: Excitation-induced dephasing and nonperturbative cavity feeding effects," Phys. Rev. Lett. **106**(24), 247403 (2011).
57. D. P. S. McCutcheon and A. Nazir, "Quantum dot Rabi rotations beyond the weak exciton–phonon coupling regime," New J. Phys. **12**(11), 113042 (2010).
58. A. Strathearn, B. W. Lovett, and P. Kirton, "Efficient real-time path integrals for non-Markovian spin-boson models," New J. Phys. **19**(9), 093009 (2017).
59. M. Cosacchi, M. Cygorek, F. Ungar, A. M. Barth, A. Vagov, and V. M. Axt, "Path-integral approach for nonequilibrium multitime correlation functions of open quantum systems coupled to Markovian and non-Markovian environments," Phys. Rev. B **98**(12), 125302 (2018).
60. M. Glässl, A. M. Barth, and V. M. Axt, "Proposed robust and high-fidelity preparation of excitons and biexcitons in semiconductor quantum dots making active use of phonons," Phys. Rev. Lett. **110**(14), 147401 (2013).
61. A. Vagov, M. D. Croitoru, M. Glässl, V. M. Axt, and T. Kuhn, "Real-time path integrals for quantum dots: Quantum dissipative dynamics with superohmic environment coupling," Phys. Rev. B **83**(9), 094303 (2011).
62. G. Hornecker, A. Auffèves, and T. Grange, "Influence of phonons on solid-state cavity-QED investigated using nonequilibrium Green's functions," Phys. Rev. B **95**(3), 035404 (2017).
63. P. Kaer, P. Lodahl, A.-P. Jauho, and J. Mork, "Microscopic theory of indistinguishable single-photon emission from a quantum dot coupled to a cavity: The role of non-Markovian phonon-induced decoherence," Phys. Rev. B **87**(8), 081308 (2013).
64. P. Kaer, T. R. Nielsen, P. Lodahl, A.-P. Jauho, and J. Mørk, "Microscopic theory of phonon-induced effects on semiconductor quantum dot decay dynamics in cavity QED," Phys. Rev. B **86**(8), 085302 (2012).
65. K. Roy-Choudhury and S. Hughes, "Spontaneous emission from a quantum dot in a structured photonic reservoir: phonon-mediated breakdown of Fermi's golden rule," Optica **2**(5), 434–437 (2015).
66. K. Roy-Choudhury and S. Hughes, "Quantum theory of the emission spectrum from quantum dots coupled to structured photonic reservoirs and acoustic phonons," Phys. Rev. B **92**(20), 205406 (2015).

Optical Materials EXPRESS

67. J. Iles-Smith, D. P. S. McCutcheon, J. Mørk, and A. Nazir, "Limits to coherent scattering and photon coalescence from solid-state quantum emitters," Phys. Rev. B **95**(20), 201305 (2017).
68. J.-Y. Marzin and G. Bastard, "Calculation of the energy levels in InAs/GaAs quantum dots," Solid State Commun. **92**(5), 437–442 (1994).
69. C. Pryor, "Eight-band calculations of strained InAs/GaAs quantum dots compared with one-, four-, and six-band approximations," Phys. Rev. B **57**(12), 7190–7195 (1998).
70. A. Franceschetti and A. Zunger, "Direct pseudopotential calculation of exciton Coulomb and exchange energies in semiconductor quantum dots," Phys. Rev. Lett. **78**(5), 915–918 (1997).
71. A. Nysteen, P. Kaer, and J. Mork, "Proposed quenching of phonon-induced processes in photoexcited quantum dots due to electron-hole asymmetries," Phys. Rev. Lett. **110**(8), 087401 (2013).
72. J. Blakemore, "Semiconducting and other major properties of gallium arsenide," J. Appl. Phys. **53**(10), R123–R181 (1982).
73. M. Cardona and N. E. Christensen, "Acoustic deformation potentials and heterostructure band offsets in semiconductors," Phys. Rev. B **35**(12), 6182–6194 (1987).
74. H. Choi, D. Zhu, Y. Yoon, and D. Englund, "Cascaded cavities boost the indistinguishability of imperfect quantum emitters," Phys. Rev. Lett. **122**(18), 183602 (2019).
75. F. Peyskens and D. Englund, "Quantum photonics model for nonclassical light generation using integrated nanoplasmonic cavity-emitter systems," Phys. Rev. A **97**(6), 063844 (2018).
76. S. Stobbe, T. Schlereth, S. Höfling, A. Forchel, J. M. Hvam, and P. Lodahl, "Large quantum dots with small oscillator strength," Phys. Rev. B **82**(23), 233302 (2010).
77. E. Hanamura, "Very large optical nonlinearity of semiconductor microcrystallites," Phys. Rev. B **37**(3), 1273–1279 (1988).
78. P. Tighineanu, R. S. Daveau, T. B. Lehmann, H. E. Beere, D. A. Ritchie, P. Lodahl, and S. Stobbe, "Single-photon superradiance from a quantum dot," Phys. Rev. Lett. **116**(16), 163604 (2016).
79. S. Stobbe, P. T. Kristensen, J. E. Mortensen, J. M. Hvam, J. Mørk, and P. Lodahl, "Spontaneous emission from large quantum dots in nanostructures: Exciton-photon interaction beyond the dipole approximation," Phys. Rev. B **86**(8), 085304 (2012).
80. A. Alkauskas, B. B. Buckley, D. D. Awschalom, and C. G. V. de Walle, "First-principles theory of the luminescence lineshape for the triplet transition in diamond NV centres," New J. Phys. **16**(7), 073026 (2014).
81. Z.-X. Koong, D. Scerri, M. Rambach, T. S. Santana, S.-I. Park, J. D. Song, E. M. Gauger, and B. D. Gerardot, "Fundamental limits to coherent photon generation with solid-state atom-like transitions," Phys. Rev. Lett. **123**(16), 167402 (2019).
82. A. J. Brash, J. Iles-Smith, C. L. Phillips, D. P. S. McCutcheon, J. O'Hara, E. Clarke, B. Royall, J. Mørk, M. S. Skolnick, A. M. Fox, and A. Nazir, "Light scattering from solid-state quantum emitters: Beyond the atomic picture," Phys. Rev. Lett. **123**(16), 167403 (2019).
83. O. Černotík, A. Dantan, and C. Genes, "Cavity quantum electrodynamics with frequency-dependent reflectors," Phys. Rev. Lett. **122**(24), 243601 (2019).
84. E. V. Denning, J. Iles-Smith, and J. Mork, "Quantum light-matter interaction and controlled phonon scattering in a photonic fano cavity," arXiv preprint, arXiv:1907.13423 (2019).
85. S. Lüker and D. E. Reiter, "A review on optical excitation of semiconductor quantum dots under the influence of phonons," Semicond. Sci. Technol. **34**(6), 063002 (2019).
86. A. Carmele and S. Reitzenstein, "Non-Markovian features in semiconductor quantum optics: quantifying the role of phonons in experiment and theory," Nanophotonics **8**(5), 655–683 (2019).